Towards optimized illumination for high-resolution ptychography

MICHAL ODSTRČIL,[1,*] MAXIME LEBUGLE,[2] MANUEL GUIZAR-SICAIROS,[1] CHRISTIAN DAVID,[2] AND MIRKO HOLLER[1]

[1] *Swiss Light Source, Paul Scherrer Institute, Villigen 5232, Switzerland*
[2] *Laboratory for Micro and Nanotechnology, Paul Scherrer Institute, Villigen, Switzerland*
[*] *michal.odstrcil@psi.ch*

Abstract: We present a systematic study, where effects of the illumination probe design on ptychography reconstruction quality are evaluated under well-controlled conditions. The illumination probe was created using Fresnel zone-plate (FZP) optics with locally displaced zones to provide a fine control over perturbations of the illumination wavefront. We show that optimally designed wavefront modulations not only reduce bias and variance in the reconstruction of the lowest spatial frequencies but also lead to improved imaging resolution and reduction of artefacts compared to a conventional FZP. Both these factors are important for quantitative accuracy and resolution of ptychographic tomography. Our work furthers the understanding of the important characteristics of an optimal illumination for high-resolution X-ray ptychography and how to design optimal FZP wavefront modulations for different applications of ptychographic imaging. These findings are applicable and relevant for ptychography using optical, EUV, and X-ray photons as well as electrons.

1. Introduction

In the last decade, ptychography has become a standard and a very successful method for high-resolution quantitative imaging in X-ray [1–6], extreme ultraviolet (EUV) [7,8] and optical wavelength range [9–11] and in electron microscopy [12–14]. Conventional ptychography is a scanning-based coherent diffractive imaging (CDI) method that provides very robust and accurate phase-retrieval. The high robustness is achieved by the use of the translation diversity provided by lateral shifting of the sample with respect to a structured illumination probe. The measured diffracted intensities combined with additional information from the adjacent, partly overlapping scan regions are used to recover the complex-valued sample transmissivity or reflectivity. Since there are no optics required between the sample and the detector and every photon is collected in parallel by an area detector, it provides a way for dose efficient imaging [3, 15–17], and it can provide sub-15 nm resolution with X-ray photons [4,5,18] and deep sub-ångström resolution with electrons [13]. An important feature of ptychography is the ability to recover additional variables along with the sample transmissivity such as the complex-valued illumination probe [2,9,19,20] and its time evolution [21,22], relative positions of the sample with respect to the illumination probe [19,22–25], coherence properties of the illumination [26], spectral information [27], and many others [22,28–31]. This flexibility alleviates the need for perfect experimental conditions, such as precise knowledge of the illumination wavefront, and makes ptychography a valuable tool for beam characterization and aberration sensing [32–38].

Although ptychography reconstruction algorithms do not need to be provided with a precisely known illumination probe, the illumination still needs to satisfy several constraints. In order to reach optimal performance, conventional scanning-based ptychography requires a constant and sufficiently structured illumination probe that provides sufficient translation diversity. Additionally, in the particular case of conventional far-field ptychography, the illumination probe must have a limited spatial extent in order to provide adequate sampling of the far-field diffraction pattern.

This raises the important question of how the illumination can be tuned to improve the imaging performance, resolution, or quantitative accuracy. It also raises the question of the relevant trade-offs and compromises associated with these modifications. The most common approaches to create the illumination probe for the X-ray ptychography are either a beam limiting pinhole [1,3] or a focusing element such as Fresnel zone plates (FZPs) [2, 18, 33, 39–41], Kirkpatrick-Baez (KB) mirrors [32, 36], or refractive lenses [34, 42]. Nowadays, a focused beam illumination is the dominant choice for high-resolution X-ray ptychography due to longer working distance, and the reduced dynamic range in the collected diffraction patterns. Additionally, the focused illumination allows for tuning the extent of the illumination probe simply by moving the sample along the direction of the beam propagation [33].

The idea of optimizing the illumination wavefront for ptychography was already studied both numerically [43–46] and experimentally with various approaches [10, 47–51]. The techniques for illumination probe optimization for ptychography can be broadly classified in two distinct approaches. The first approach, adopted by most of the studies, attempts to broaden the spatial frequency content of a focused illumination, *i.e.* effectively its coverage of the far-field detector, with the goal to reduce the dynamic range of the collected diffraction patterns [10, 48] and to enhance the ptychographic translation diversity [47]. Since ptychography is principally a structured illumination technique, the additional structure in the illumination provides stronger information, when a probe shift is performed, one way to intuitively understand this is by going to the opposite extreme, namely if the illumination has no structure then translations are inconsequential. A more structured illumination leads to better convergence [44, 45], higher reconstruction quality [47] and better modal decomposition [50]. Enhancement of the spatial frequency content can be done either by adding a hard edge [47] or a diffuser-like element between the focusing optics and the sample [10, 48, 49]. However, the beam modulator needs to be placed very close to the sample, in order to avoid significant increase of the illumination probe diameter. The resulting small working distance limits the applicability of this approach for high-resolution ptychography.

The second approach is to place a wavefront perturbation element upstream or directly into the focusing optics. This option was first experimentally demonstrated in the context of the X-ray ptychography in [51]. However, their implementation leads to extremely strong aberrations and severe broadening of the illumination probe that, as we will show, may deteriorate the reconstruction quality. In order to prevent various drawbacks caused by broadening of the illumination probe, the amplitude and spatial frequencies of the fabricated wavefront perturbations have to be optimized [45]. Additionally, this approach does not reduce data dynamic range nor does it broaden the illumination spectrum compared to an aberration-free focusing optics. A wavefront perturbation element placed near or at the lens plane cannot broaden illumination at the detector plane without significant extending of the illumination size at the sample plane. A weak aberration element placed near or at the lens plane cannot broaden illumination at the detector plane because the footprint of the illumination on the detector is solely determined by the lens numerical aperture, which is not modified significantly by weak aberrations. Therefore, fabrication of wavefront modulations directly into the FZP does not share the same effect on the measurement and reconstruction as the aforementioned diffuser-near-the-sample approach.

Here we study the second approach, namely the effects and the optimal wavefront modulation to be designed directly into the FZP pattern. This approach allows us to preserve the working distance of the used focusing optics. Additionally, the direct integration of the wavefront modulation into the FZP eliminates possible drifts between multiple optical elements and the transmission efficiency of the focusing optics is preserved. Our goal is to present a systematic study based on well-controlled amplitude and spatial frequencies of the wavefront modulation to design an improved ptychographic illumination. For easier comparison, all measurements were done with the same experimental parameters: the FZPs have identical diameter, focal length, and

all measurements are done with the same sample to optics distance. Therefore we avoid effects caused by varying illumination NA, illumination diameter on the sample, transmission efficiency, and coherent fraction.

2. Design and manufacture of FZPs with wavefront modulation

We designed and fabricated 9 gold FZPs with different wavefront modulation properties, at the Laboratory of Micro and Nanotechnology, Paul Scherrer Institut, Switzerland. All FZPs have a diameter of 170 μm, a structure height of 1.1 μm, and the outermost zone width of 60 nm. The FPZs were electroplated in polymethyl methacrylate (PMMA) molds patterned using an e-beam lithography writer (Vistec EBPG 5000plus). As reported in previous works [52, 53], the concentric rings of the FZP are cut into smaller arcs to avoid the collapse of the PMMA, molds during intermediate steps in the process. Each of the tested zone plates contains a different level of high-order aberrations defined by a smoothly varying random displacement vector field (DVF) with a Gaussian probability distribution determined by a characteristic spatial frequency k_a, *i.e.*, spatial period of $\lambda_a = 2\pi/k_a$. The DVF was applied to distort both the vertical and horizontal coordinates of each FZP element, *i.e.* to deform the Fresnel zones. The expected additional wavefront phase modulation can be then estimated as

$$\Phi(\mathbf{x}) = [\Delta X_{\mathrm{DVF}}(\mathbf{x}) + \Delta Y_{\mathrm{DVF}}(\mathbf{x})]/w(\mathbf{x}) \tag{1}$$

where $w(\mathbf{x})$ describes the local average width of the Fresnel zones at the position $\mathbf{x}$ and ΔX_{DVF} and ΔY_{DVF} are horizontal and vertical components of the deformation field. Although the shift of the zones was up to ±90 nm with respect to their original position, the width of the outermost zone width varies only within a range of ±10% from its nominal value. The maximum designed amplitude differences $\|\Delta\Phi\| = \max(\Phi) - \min(\Phi)$ of the wavefront modulation and their characteristic spatial frequencies k_a are summarized in Table 1 for each of the tested FZPs. GDS schemas of the perturbed zone plates are provided in Dataset 1 [61].

Table 1. Summary of the design parameters for the tested FZPs. The characteristic spatial frequency is denoted by k_a [μm^{-1}] and the maximal amplitude difference of the FZP modulations by $\|\Delta\Phi\|$ [rad].

# FZP	k_a	$\|\Delta\Phi\|$	# FZP	k_a	$\|\Delta\Phi\|$	# FZP	k_a	$\|\Delta\Phi\|$
11	-	-	21	1.2	1π	31	2.0	1π
21	0.4	2π	22	1.2	2π	32	2.0	2π
31	0.4	3π	23	1.2	3π	33	2.0	3π

FZP11, which served as a reference, is a standard zone plate with no additional wavefront perturbations. The other FZPs contain fabricated well-controlled aberrations with different amplitudes and dominating spatial frequencies. The coordinate deformations of the produced FZPs can be observed as distortions of the Moire effect in Fig. 1(g). Note that the presented characteristic spatial frequency k_a, is relevant only for the FZP diameter of 170 μm. In order to reproduce our results with a FZP of a different diameter, the characteristic spatial period should be scaled proportionally to the FZP diameter in order to maintain number of the spatial periods over the pupil size. Given the FZP diameter of 170 μm and perturbations with spatial frequencies of $k_a = \{0.4, 1.2, 2.0\}$ μm^{-1}, the average number of spatial periods over the pupil diameter is equal to 10.8, 32.5 and 54.1 respectively.

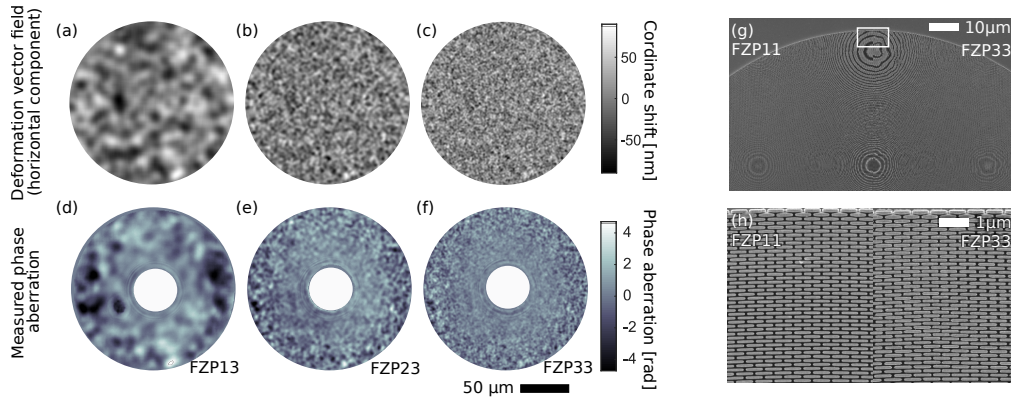Fig. 1. Images (a-c) show horizontal components ΔX_{DVF} of the designed DVF for each of the tested spatial frequencies k_a in Table 1 and maximal DVF amplitude of 180 nm. Images (d-f) show corresponding measured wavefront aberrations for FZP13, 23 and 33 after subtraction of the reference aberration-free phase wavefront measured on the reference FZP11. The white regions in centers of the images (d-f) could not be measured due to the central stop. Image (g) shows a scanning electron microscopy (SEM) image of FZP11 (left) and FZP33 (right), where the Moire pattern between the SEM scanning lines and the zone structures clearly highlights the irregularities of the local zone widths. A detail of the zones is shown in (h).

3. Characterization of the fabricated FZPs

Characterization and tests of the FZPs were carried out using X-ray ptychography at the cSAXS beamline of the Swiss Light Source, PSI, Switzerland, using the flexible tOMography Nano Imaging (flOMNI) end-station [4]. High stability and interferometric feedback of the flOMNI end-station helps to mitigate drifts and vibrations that could otherwise deteriorate the data quality and thus affect reconstruction quality comparisons. The illumination wavefront was reconstructed by ptychography at 6.2 keV photon energy. In order to block the zero-order light, a gold central stop of 50 μm diameter was positioned upstream of the FZP and an order sorting aperture of 30 μm diameter was placed after the FZP, such that only the first diffraction order was passing to the sample. The intensity of the signal scattered by a test sample, described further in Section 5, was measured using an in-vacuum Eiger 1.5M detector [54] placed 5.268 m downstream of the sample. A detailed description of other experimental parameters can be found in Section 4.

The amplitudes of the reconstructed illumination probes for each FZP are shown in Fig. 2, where Fig. 2(a) shows amplitudes at the sample plane and Fig. 2(b) at the detector plane. These measured probe amplitudes at the detector plane are dominantly affected by a combination of 1) the non-uniform amplitude and wavefront of the incident beam due to upstream beamline optics, as can be seen in the reference FZP11 in Fig. 2(b), 2) by the controlled aberrations fabricated into the FZPs and 3) by the entrance pupil shape, *i.e.* the diameters of the FZP and of the central stop.

Figure 2(a) shows the effects of the different wavefront modulation on the reconstructed illumination probes. The aberrations with low spatial frequencies in FZP12 and FZP13 result in evident changes of the illumination probe at the sample plane compared to the reference FZP11. This is in contrast to the rather subtle change of the amplitude distribution at the detector plane shown in Fig. 2(b) compared to the reference FZP11. On the other hand, FZP22, 23, 32 and 33 provide a strong amplitude modulation at the detector plane, while the overall amplitude distribution at the sample plane is close to that of FZP11. Reconstructions of the phase modulations for FZP 13, 23 and 33 are shown in Fig. 1(d) and (f).

Figures 1(g) and 1(h) also show SEM images of the FZP11 and FZP33. The introduced shift
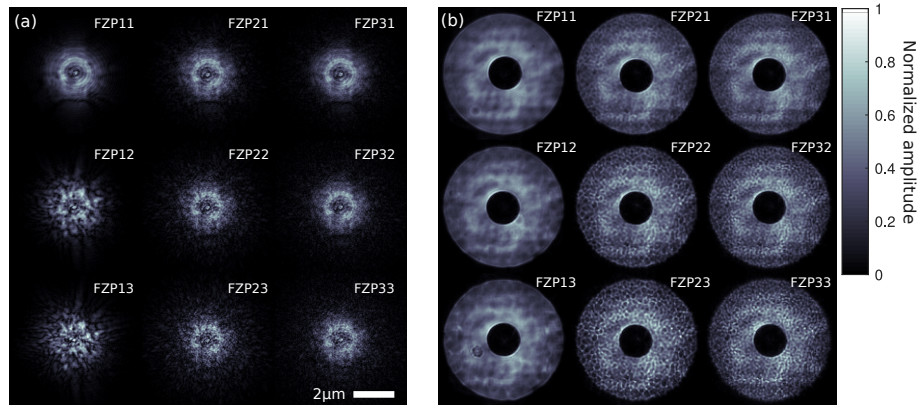
Fig. 2. Normalized amplitude of the reconstructed probes for each of the tested Fresnel zone plates listed in Table 1(a) at the sample plane and (b) at the detector plane. In (b) the dark regions in center of the propagated patterns are caused by the central stop. The images of the real-space amplitudes in (a) are cropped from $14 \times 14 \, \mu m^2$ down to $7 \times 7 \, \mu m^2$ and the far-field amplitudes in (b) were cropped down to $19 \times 19 \, mm^2$ for better visualization of the effects of the wavefront modulation.

of zones in FZP33 becomes visible as a strong irregularity of the Moire fringes in Fig. 1(g).
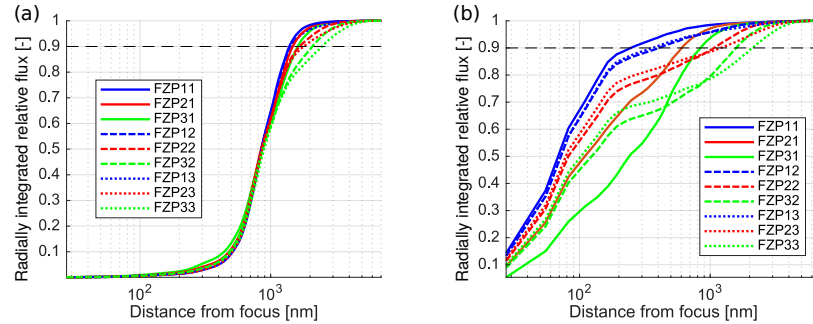

Fig. 3. Radially integrated intensity distribution (RIID), see Eq. (2), for each of the tested FZPs at the sample plane (a) and at the beam focus plane (b).

One of the potential drawbacks of the wavefront-modulated FZP is the increase of the beam waist size at the focal plane. If the increase of focus waist diameter is significant it may pose a limitation for nanoprobe-based ptychography [55], which combines X-ray ptychography with fluorescence imaging [39–41, 56]. The effects of the beam waist broadening are illustrated in Fig. 3(b) and Fig. 5. Figure 3(b) shows the radially integrated intensity distribution (RIID) in focus

$$RIID(R) = \int_0^R \int_0^{2\pi} |P_f(r, \psi)|^2 d\psi r dr \qquad (2)$$

where $P_f(r, \psi)$ denotes reconstructed illumination probe propagated to the focus. The reference FZP11 provides the tightest waist with a full width at half maximum (FWHM) of 81 nm, a Strehl ratio S=0.64, see Fig. 4, with 90% of flux contained within a diameter of 0.43 μm. However, even FZP21 and FZP31 still provide a comparable FWHM equal to 87 nm, S=0.62 and with 90% of flux is contained within a radius of 0.75 μm and 0.67 μm respectively. On the other hand, the high-amplitude and low-spatial-frequency modulations present in FZP13 lead to broadening
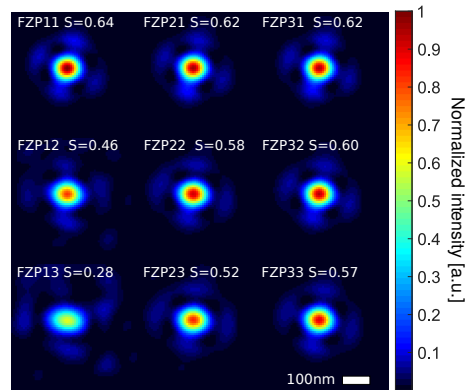
Fig. 4. Calculated beam intensity in the focal plane for each of the tested lenses with S denoting the Strehl ratio. The Strehl ratio was estimated as the ratio of the peak intensity at the focus versus the peak intensity at focus expected from an aberration-free lens.

of the beam in focus and reduce Strehl ratio to S=0.28. The FWHM of RIID equal to 423 nm would present a severe drawback for multimodal nanoprobe imaging. Wavefront modulations with finer spatial frequencies do neither significantly expand the FWHM of the RIID nor reduce the Strehl ratio, however for example the high-amplitude wavefront modulation present in FZP33 lead to a slowly decaying RIID and a diameter of 4.1 μm is required to cover 90% of the total flux, as shown in Fig. 3(b). The increase in beam waist size may significantly increase demands on ptychography data sampling at the detector plane. FWHM of RIID at the sample plane, which is placed 0.87 mm downstream the focus, is equal to 1.65 μm and, as shown in Fig. 3(a), it is practically independent of the chosen FZP.

4. Quantitative accuracy - reconstruction of the lowest spatial frequencies

Exact and unbiased reconstruction of the lowest spatial frequencies is crucial for high fidelity quantitative ptychographic tomography [57]. Although ptychography was observed to provide highly quantitative phase reconstruction over a broad range of spatial frequencies [58], phase errors can be present, when the dimensions of the reconstruction are significantly larger than the illumination probe size. Even a small repeating bias in all 2D projections will result in errors in the local refractive index and the inferred electron density. As we will show in this section, with the introduction of wavefront modulations directly on the lens we can significantly improve the reconstruction accuracy of the lowest spatial frequencies.

The test sample was a fluid catalytic cracking (FCC) catalyst particle with an approximate diameter of 20 μm. This catalyst particle provides a good test sample to assess reconstruction quality of the lowest spatial frequencies, since the required horizontal field of view is 10-times larger than the illumination probe diameter. Four identical scans of the FCC particle were acquired with each of the FZP at a photon energy of 6.2 keV. Each scan consisted of 2344 positions with an average step size of L=0.8 μm and an exposure time of 50 ms per point. The scan pattern was following a Fermat spiral trajectory [59] and covered a field of view of 50 μm×30 μm. Given the illumination probe FWHM of D_p=1.65 μm, the average linear overlap [60], defined as $1 − L/D_p$, was 51%. The diffraction patterns were collected by an in-vacuum Eiger detector 1.5M [54] placed at a distance of 5.268 m from the sample. Only the central region of 512×512 pixels of the detector was used for the reconstructions presented in this section, which results in a reconstruction pixel size of 29 nm. The average dose was on average $1.1·10^4$ photons per object pixel, *i.e.*, 15 photons/nm^2. The measured datasets are available in public repository [61] and the reconstruction codes were published in [22]. Since the reconstruction quality depends

also on the reconstruction method, we present reconstructions performed by 400 iterations of the difference map (DM) algorithm [2] with the Fourier- and real-space relaxation constants of 0.95, followed by a refinement with 200 iterations of the least-squares maximum likelihood method LSQ-ML with compact overlap subset selection [22]. Additionally for comparison, we show reconstructions using 400 iterations of the extended ptychography engine (ePIE) using $\alpha = 0.9$ and $\beta = 0.9$ as defined in [9].

Figure 5 shows four examples of the unwrapped phase reconstructions [62] of the FCC particle with two ePIE reconstructions in the top row and two DM+LSQ-ML reconstructions below. The phase ramp and phase offset were subtracted using the air along the edges of the reconstruction as reference. The dataset in Fig. 5(a) and (c), was acquired with the reference FZP11 and the dataset in Fig. 5(b) and (d), with FZP33, which has the strongest and highest-spatial-frequency modulation. The ePIE reconstruction with the reference FZP clearly leads to severe underestimation of the average phase within the sample and also results in strong halo-like artefacts in the air surrounding the sample. These problems are significantly improved when FZP33 was used in Fig. 5(b), however, the low-frequency errors are still present as it can be seen in the air around the sample, where the phase should be flat and equal to zero. The DM+LSQ-ML reconstructions show a significant improvement in the recovery of the lowest spatial frequencies for the reference FZP compared to the ePIE reconstructions, as can be seen comparing Fig. 5(a) and Fig. 5(c). However, even in this case, the wavefront modulation further reduces the low-spatial-frequency variations of the phase in the air region as shown in Fig. 5(d).
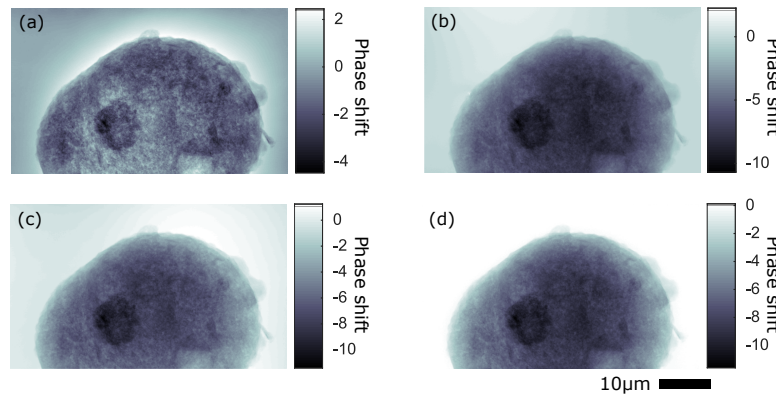

Fig. 5. Unwrapped phase of a reconstruction from a fluid catalytic cracking (FCC) catalyst particle. Images (a,b) show reconstructions using ePIE, (c,d) shows the same datasets reconstructed by DM+LSQ-ML. The dataset used in (a,c) was acquired with the reference FZP11, while the dataset in (b,d) was acquired with the FZP33, which has wavefront modulations of the highest amplitude and spatial frequency. The color scale was selected to cover the full range of the phase values for each reconstruction separately. The phase ramp and phase offset were subtracted. Line cuts though the reconstructed phase are presented in Fig. 6.

A more quantitative overview of these results can be seen in Fig. 6, where a line cut though the phase reconstructions is depicted. Figure 6(a) shows a horizontal cut through the center of the reconstructions and Fig. 6(b) a horizontal cut through air. In Fig. 6(b), only the DM+LSQ-ML reconstruction are plotted for the sake of visibility. The shaded areas in Fig. 6(a) and (b) denote the standard deviation of the recovered phase for four subsequently measured datasets. Using wavefront-modulated FZPs not only removed the average bias of the reconstructed low-frequency phase in the air region as shown in Fig. 6(b), but it also reduces the phase variation between independent reconstructions. Similar reduction of the variation can also be seen in the cut though

the sample in Fig. 6(a). Although the ground truth phase in Fig. 6(a) is not known, based on the phase reconstruction in air, we assume that the phase reconstruction using the perturbation-free FZP with a DM+LSQ-ML reconstruction led to a phase underestimation by up to 8%.
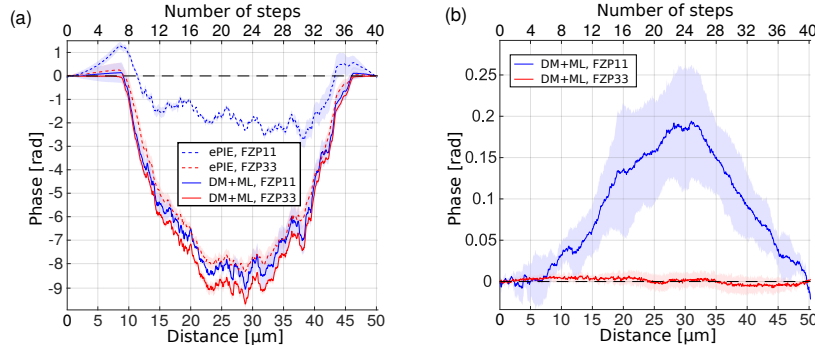

Fig. 6. Visualization of horizontal cuts through the reconstructions depicted in Fig. 5, (a) cut through center of the FCC particle, and (b) cut through the air region above the sample. The lines correspond to the average phase and the shaded areas to the standard deviation calculated from four subsequent ptychographic scans of the catalyst particle that were reconstructed independently.

Table 2. Root mean squared (RMS) value of the phase in air

FZP	_1	_2	_3
1_	0.48	0.32	0.27
2_	0.39	0.12	0.05
3_	0.35	0.06	**0.04**

Table 3. Average number of phase residues [62] in each reconstruction

FZP	_1	_2	_3
1_	**0**	0.25	0.25
2_	0.75	**0**	**0**
3_	1	**0**	**0**

Tables 2-5 shows performance metrics to assess more quantitatively the DM+LSQ-ML reconstructions with each FZP. The best results are marked in bold. Reconstructions from the reference FZP11 show the largest residual phase error in the air regions as shown in Table 2. It should be noted that the low-spatial-frequency wavefront modulations in FZP12, 13 do not lead to a notable quality improvement despite the significant effect on the illumination probe that can be seen in Fig. 2(a). These low-spatial-frequency wavefront perturbations in FZP12 and FZP13 produce also more unevenly distributed illuminations on the sample. This is shown in Table 4 by means of the relative standard deviation of the illumination function defined as

$$I_{\text{tot}}(\mathbf{x}) = \sum_i |P(\mathbf{x} + \mathbf{x}_i)|^2 \quad , \tag{3}$$

Table 4. Relative variation of the local dose, defined in Eq. (3)

FZP	_1	_2	_3
1_	**14%**	15%	15%
2_	24%	18%	16%
3_	27%	20%	17%

Table 5. Reciprocal space roughness defined in Eq. (4) normalized by value of the FZP11.

FZP	_1	_2	_3
1_	1.00	1.64	2.25
2_	1.05	3.42	5.81
3_	1.22	6.78	**11.55**

where P denotes the complex-valued illumination probe, $\mathbf{x}$ are the real-space coordinates and $\mathbf{x}_i$ is the i-th scan position. This uneven illumination could explain why the reconstructions from FZP12 and FZP13 result more often in phase residues [62], as shown in Table 3. Presence of phase residues and vortices in the reconstructed field of view means that there is no unique phase unwrapping, which results in ambiguity of the phase reconstruction and potential artefacts in the ptycho-tomographic reconstruction. Finally, the values of the reciprocal amplitude roughness of the diffraction cone, shown in Table 5, were determined as

$$R = \sum_{\mathbf{k}} \left[(\nabla_{\mathbf{k}_x} |P_d|)^2 + (\nabla_{\mathbf{k}_y} |P_d|)^2 \right] \quad , \tag{4}$$

where $|P_d|$ denotes the probe amplitude at the detector plane and $\nabla_{\mathbf{k}_x}$, $\nabla_{\mathbf{k}_y}$ are directional gradients. The reciprocal amplitude roughness express the spatial variability of the far-field probe amplitude and its importance will be discussed in Section 6.

5. Image quality

In order to compare the image quality produced from each FZP, while reducing potentially limiting factors such as the depth of field [31], we used a spokes test structure lithographically made from hydrogen silsesquioxane resist (HSQ) and coated with 10 nm layer of iridium using atomic layer deposition [63]. The exposure time per scan position was reduced down to 10 ms and the field of view of the scan was reduced to $20\times20\,\mu m^2$. The pixel size in the object plane was limited by the detector extent to 10 nm. Other scan parameters such as the scan step or the probe diameter were identical to the previous measurements of the catalyst particle. The resulting imaging dose was 414 photons per object pixel, *i.e.* 2.9 photons per nm^2. The measured datasets are available in a public repository [61].

The reconstruction was performed with 400 iterations of DM and 400 iterations of LSQ-ML. Due to the very short exposure time of 10 ms, fast vibrations with a period of about 25 ms, caused by the cryogenic cooling system of the X-ray monochromator at the cSAXS beamline, resulted in quasi-random variations of the illumination probe between subsequent scan positions. Therefore, we have additionally used LSQ-ML with the orthogonal probe relaxation [21,22]. Two additional orthogonal probe modes were used to account for variations of the probe wavefront. An example of the time evolution of the probe reconstruction is shown in Visualization 1. The resulting relative standard deviation of the far-field intensity of the variable illumination probe was 11%.

Figures 7(a) and 7(c) show examples of the conventional ptychographic reconstruction and Figs. 7(b) and 7(d) show the ptychographic reconstruction with the two additional OPR modes.
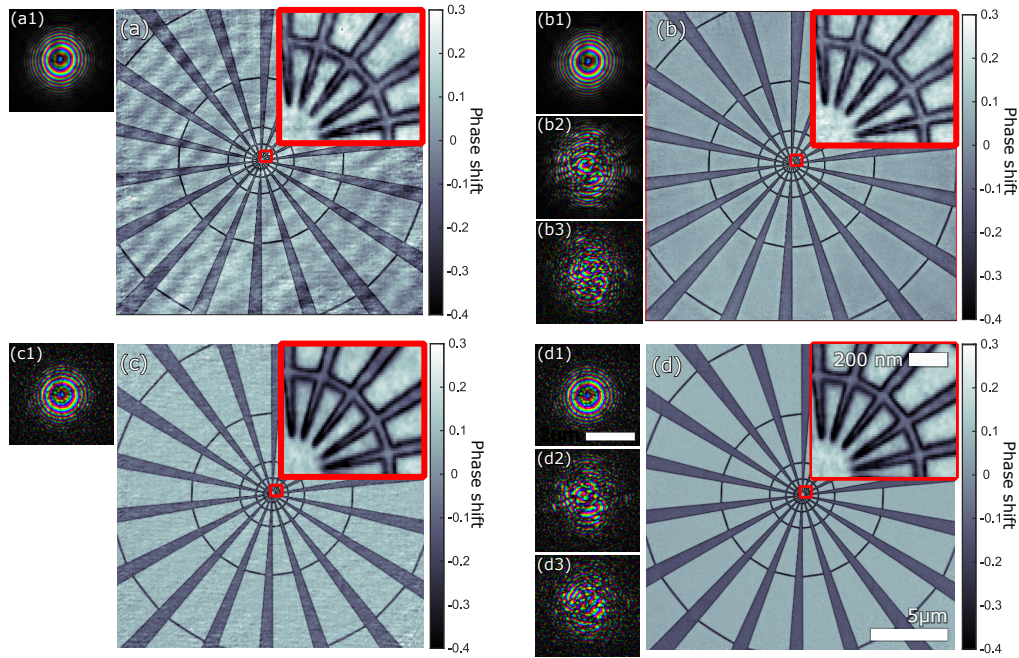

Fig. 7. Examples of the Siemens star reconstructions with FZP11 (a,b) and with FZP33 (c,d). Conventional single-probe ptychography reconstructions by the LSQ-ML method are shown in (a,c) and identical datasets reconstructed by the LSQ-ML method with additional two orthogonal relaxation modes are shown in (b,d). Insets show in detail the center of the Siemens star. The illumination probes reconstructed using a single-mode algorithm for FZP11 and FZP33 are shown in (a1) and (c1), respectively. Sub-images (b1-b3) and (d1-d3) contain three principal components used to describe temporal evolution of the illumination probes via the orthogonal probe relaxation [21]. Visualization 1 demonstrates the reconstructed temporal evolution of probes in (b1-b3,d1-d3) and its corresponding far-field intensity pattern.

Four ptychographic scans were acquired for each illumination configuration, allowing us to use six different combinations of two scans to evaluate relative repeatability of the measurement and reconstruction process using Fourier ring correlation (FRC) between two independent ptychographic scans. High repeatability and reliability of the reconstruction quality are important parameters that directly affect the resolution of ptychographic tomography, for which hundreds of high-resolution artifact-free projections are required.

As shown in Fig. 3, the introduction of wavefront modulation into the FZP spreads the beam footprint at the sample plane, *i.e* the region with non-negligible beam intensity, which directly affects the requirements of far-field sampling. To investigate this, the effect of detector intensity sampling on the reconstruction quality was evaluated by binning the measured data. This allows us to compare ptychography reconstructions with a sampling that would be obtained by placing the detector closer to the sample. Since the focused illumination probes do not have a clearly defined support, we define the illumination probe diameter as the FWHM of the integral flux curve in Fig. 3(b), therefore the probe FWHM of $D_p = 1.65\,\mu m$ would result for the unbinned dataset in a linear sampling ratio of $Q = D_a/D_p = 8.5$, where D_a denotes the total reconstructed extent of the probe field of view. Binning reduces the sampling ratio to 4.2 and 2.1 for binning

2×2 and 4×4 pixels, respectively, which is equivalent to reducing sample to detector distance from 5.27 m to 2.63 m and 1.31 m. We have selected only 3 FZPs for our analysis: FZP11 as a reference zone plate, FZP22 with a moderate wavefront aberration amplitude and spatial frequency and finally FZP33 with a strong and highest spatial frequency aberrations resulting in a more significant portion of the intensity to be located outside of the illumination function as shown in Fig. 3(a). Results of our resolution tests are presented in Fig. 8, where the intersection of the average FRC curve with the 1-bit threshold [64] is used to define the resolution.
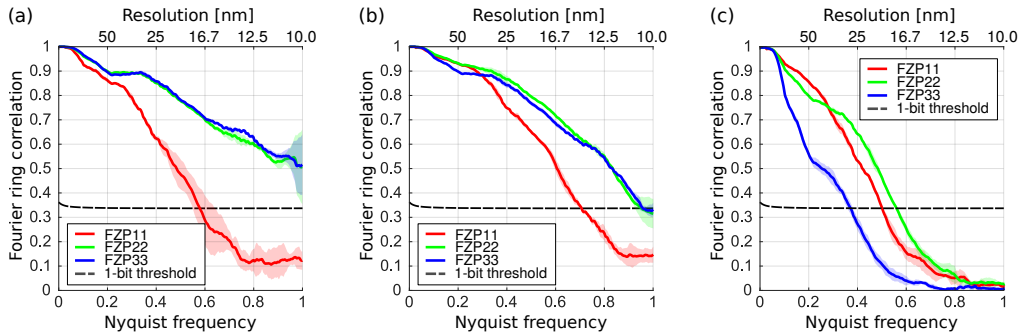

Fig. 8. Reconstruction quality comparison for a spokes test sample for different levels of wavefront modulation and sampling. Plots (a-c) show reconstructions for detector pixels binning of 1×1, 2×2 and 4×4 pixels respectively.

The reference FZP11 (red line) produces similar results for different sampling, with the highest resolution of 14.1 nm reached in the 2×2 binned dataset. Compared to the reference FZP11, the FZPs with wavefront modulation provide significant improvement in the resolution. This is most significant for the unbinned dataset, where the repeatable resolution was reached down to the pixel-size limit of 10 nm compared to a resolution of 17.1 nm for the reference optics. For the 2×2 binning, the resolution of the perturbated optics is just slightly below the pixel limit at 10.3 nm. Finally, in the case of the 4×4 binned dataset, the reconstruction quality dropped for all the tested FZP as shown in Fig. 8(c). This quality reduction was most significant for the strongly perturbated FZP33, for which the repeatable resolution was reduced to 28 nm.

6. Discussion

We have demonstrated that the convergence, quantitative accuracy, and accuracy of the reconstruction low-spatial-frequencies can be improved by introducing well-controlled aberrations into the illumination focusing lenses, in our case FZPs.

The principle behind this improvement can be understood from the following geometric argument. Low spatial frequencies in the object corresponding to features with a period larger than the illumination diameter, can be locally described as a phase-ramp. Since a phase-ramp in object space results in a shift in reciprocal space, ptychography is tasked with tracking the movement of the illumination in reciprocal space with deep sub-pixel precision in order to accurately recover the lowest spatial frequencies of the object. Therefore, improved accuracy can be reached either by 1) providing measurements with higher signal-to-noise ratio, *i.e.* higher dose onto the sample, or 2) by the introduction of high contrast structure into the diffracted cone. This is similar to the task of the speckle tracking imaging [65] and near-field ptychography [49], where it has already been shown that the optimal results are obtained when the speckles provide the maximal visibility [49, 66].

In order to reach improved quantitative accuracy, accurate reconstruction of the lowest spatial frequencies of the object phase is essential. Since smooth phase gradients result mainly in displacements of the far-field diffraction cone, ptychographic quantitative accuracy depends on

sensitivity towards these shifts. The effect of a small reciprocal shift, α, of the illumination probe amplitude at the detector plane $|P_d|$ along direction $\mathbf{k}_x$ can be quantified by the amplitude cost function χ^2 [29] as

$$\chi^2(\alpha) = \lim_{\alpha \to 0} \sum_{\mathbf{k}} \left[|P_d|(\mathbf{k}) - |P_d| \left(\mathbf{k} + \alpha \frac{\mathbf{k}_x}{\|\mathbf{k}_x\|} \right) \right]^2 = \alpha^2 \sum_{\mathbf{k}} (\nabla_{\mathbf{k}_x} |P_d|)^2 . \tag{5}$$

Notice that the last term in Eq. (5) is proportional to our definition of the reciprocal space roughness R in Eq. (4). Assuming the horizontal roughness $\sum_{\mathbf{k}} (\nabla_{\mathbf{k}_x} |P_d|)^2$ and the vertical roughness $\sum_{\mathbf{k}} (\nabla_{\mathbf{k}_y} |P_d|)^2$ to be comparable, displacement of the far-field amplitude by distance α from the initial position $\mathbf{k}$ will increase the cost function χ^2 by value of $\alpha^2 R$. Therefore, the quantitative accuracy of the phase is directly influenced by the Fourier domain amplitude roughness R. The fact that the reciprocal space roughness R is directly responsible for the improved low spatial frequency sensitivity can also be seen from the high correlation of 97.7% between the residual phase errors reported in Table 2 and the inverse relation to the reciprocal amplitude roughness R. Values of R are reported in Table 5. Due to its direct influence on the quantitative accuracy in ptychographic tomography, we consider that the main advantage of the lenses with wavefront modulation is the increased accuracy of the reconstruction of the low-spatial-frequencies.

Additionally, we observed improved spatial resolution in our reconstructions, which is less straightforward to explain. As mentioned in Section 5, the increase of the FRC resolution seems not to be related to the observations in [43–45, 47], where broadening the spectral distribution of the illumination by enlarging its coverage on the detector resulted in a resolution improvement given the same photon dose. For the case of lenses with wavefront modulation, the numerical aperture of the incident beam is not increased, as shown in Fig. 2(b). The observed improvement in resolution could presumably be caused by a more optimal reconstruction of the low and middle spatial frequencies, which consequently help the reconstruction algorithms converge for the highest spatial frequencies. Additional structure in the beam could also make the optimization-based methods such as maximum-likelihood [29] more robust against stagnation in local minima, and thus more suited to find a better solution. However, this effect would deserve further detailed investigation. An additional advantage of the wavefront-modulated lenses is their ability to partially suppress effects of the variable incident wavefront as it can be seen from the difference between Figs. 7(a) and 7(c). This is most likely caused by the additional structure in the propagated probe, as shown in Visualization 1, which is only mildly affected by the variable illumination probe and thus it better constraints the ptychography reconstruction. This feature of the wavefront-modulated lenses is advantageous for example when variations of the illumination probe are caused by motion of the illumination optics [67, 68]. If the beam wavefront upstream the FZP is not sufficiently smooth, the relative shift of the incident beam with respect to the FZP will result in changes of the illumination probe in a similar way to the wavefront variations observed in our measurements.

However, not all properties of the wavefront-modulated FZPs are beneficial. In particular, strong wavefront modulations may result in significant broadening of the beam waist. This not only limits applications of strongly wavefront-modulated FZPs for nanoprobe ptychography, but also leads to less evenly distributed energy of the illumination function shown in Table 4, which may result in sub-optimal reconstruction quality [44]. Also as shown in Table 3, we have observed that high-amplitude low-spatial-frequency wavefront modulations present in FZP12 and FZP13 lead more likely to residua in the reconstruction which prevent us to obtain a unique phase unwrapping [62]. Furthermore, large amplitude wavefront modulations with higher spatial frequencies lead to an increase of the sampling requirement. Therefore, the choice of the optimal aberration spatial frequencies should be based on the minimal targeted illumination size.

7.   Conclusion and Outlook

Our study demonstrates the imaging improvements obtained by integration of wavefront modulation into focusing optics for ptychography. Even with low-amplitude wavefront modulations, we already observe a significant improvement in the phase-retrieval accuracy. We have shown that the improved accuracy of the phase reconstruction has high correlation of 97.7% with the reciprocal space amplitude roughness of the wavefront aberration, as summarized in Table 5. Since the roughness depends on the amplitude and the spatial frequency of the lens perturbations, an increase of any of these parameters leads to further improvement. However, it also results in beam waist broadening, more stringent detector intensity sampling requirements, and less uniform sample illumination function. If the sampling conditions are not satisfied, an wavefront-modulated FZP can lower the reconstruction quality compared to a conventional one as shown in Fig. 8(c). The observed deterioration of the reconstruction quality is caused in this case by reduced contrast of the far-field speckles due to insufficient sampling of measured diffraction patterns. The effect on the diffraction patterns is equivalent to having lower coherent fraction in the illumination beam and it can be partially alleviated by reconstructing multiple coherent modes [26], however such approach comes at the price of signal-to-noise ratio in the reconstruction, increased overlap in the real-space domain would be required to preserve the reconstruction quality [44, 69].

Finally, we have observed that wavefront-modulated illumination lenses lead to improved spatial resolution despite the fact that the spatial frequency range of the illumination probe is almost identical to perturbation-free FZP.

Integration of the wavefront modulation directly into the illumination focusing lens has also important experimental advantages that make this approach more suitable for high-resolution X-ray ptychography compared to approaches based on a separated aberration, or diffuser, optical element placed close to the sample:

1. For cases where a diffuser is placed near the sample, its position stability should be kept constant below the sought resolution level. This means that for high-resolution ptychography an active interferometric feedback on this additional element may be needed.

2. The working distance with a diffuser close to the sample plane is determined by its characteristic scattering power, in order to satisfy the beam diameter constraint at the sample plane so that the diffraction pattern is measured with adequate sampling. Therefore, for cases of interest in high-resolution X-ray microscopy the maximal working distance can be merely in the order of tens of microns. By introducing controlled wavefront aberrations in the illumination lens we preserve the focal and working distance.

In the next steps, we plan to locally optimize the average amplitude of the deformation vector field used to modify the FZP zones structure and make it proportional to the local average zone width. This will result in a more uniform amplitude of the wavefront modulations over the entire FZP lens which helps to produce a more consistent high-visibility speckle-like pattern over the entire diffraction cone. This should make it possible to even further improve sensitivity towards sub-pixel shift of the diffraction cone without significant increase the sampling requirements. Our FZP deformation approach is fully compatible with the fabrication of the interlaced FZP optics for increased numerical aperture with high efficiency [70, 71], which will become important for reaching sub-5 nm resolution. Another application, where the wavefront-modulated lenses may become essential, are fast ptychographic scanners, where the illumination forming optics is moved with respect to a structured beam [67]. As we have shown in Fig. 7(c), the additional structure the far-field intensity significantly helps to mitigate artefacts caused by nonuniform wavefront structure upstream of the focusing optics.

The applications of optimally designed wavefron aberrations, or modulations, in optics is not only limited to X-ray ptychography with Fresnel zone plates, which as we have shown, allow to

accurately control the wavefront modulation through a local displacement of the Fresnel zones without affecting the diffraction efficiency of the FZP. Custom controlled aberrations can also be introduced in refractive or reflective X-ray optics using a designed phase plate as that in [42], both in the X-ray and EUV range.

Our conclusions are valid also for electron beam ptychography [12–14], in which the illumination wavefront modulation could be created by higher-order multipoles [72, 73], micromachined einzel lenses [74], or similarly to the presented example for X-ray, the custom aberrations can be designed into focusing optics fabricated by focused ion beam [75, 76].

The idea of an optimally aberrated optics can be also used improve the convergence of Fourier ptychography [77, 78], in which the perturbations can be directly manufactured into the imaging lens, or a liquid crystal or injection molded plastic lenses can be used to introduce weak and well-controlled aberrations into the embedded pupil function.

Acknowledgment

References

1. J. M. Rodenburg and H. M. Faulkner, "A phase retrieval algorithm for shifting illumination," Appl. Phys. Lett **85**, 4795–4797 (2004).
2. P. Thibault, M. Dierolf, A. Menzel, O. Bunk, C. David, and F. Pfeiffer, "High-resolution scanning X-ray diffraction microscopy," Science **321**, 379–382 (2008).
3. M. Dierolf, A. Menzel, P. Thibault, P. Schneider, C. M. Kewish, R. Wepf, O. Bunk, and F. Pfeiffer, "Ptychographic X-ray computed tomography at the nanoscale," Nature **467**, 436–439 (2010).
4. M. Holler, A. Diaz, M. Guizar-Sicairos, P. Karvinen, E. Färm, E. Härkönen, M. Ritala, A. Menzel, J. Raabe, and O. Bunk, "X-ray ptychographic computed tomography at 16 nm isotropic 3D resolution," Sci. Rep. **4**, 3857 (2014).
5. M. Holler, M. Guizar-Sicairos, E. H. Tsai, R. Dinapoli, E. Müller, O. Bunk, J. Raabe, and G. Aeppli, "High-resolution non-destructive three-dimensional imaging of integrated circuits," Nature **543**, 402–406 (2017).
6. F. Pfeiffer, "X-ray ptychography," Nat. Photonics **12**, 9–17 (2018).
7. M. D. Seaberg, B. Zhang, D. F. Gardner, E. R. Shanblatt, M. M. Murnane, H. C. Kapteyn, and D. E. Adams, "Tabletop nanometer extreme ultraviolet imaging in an extended reflection mode using coherent fresnel ptychography," Optica **1**, 39–44 (2014).
8. D. F. Gardner, M. Tanksalvala, E. R. Shanblatt, X. Zhang, B. R. Galloway, C. L. Porter, R. Karl Jr, C. Bevis, D. E. Adams, H. C. Kapteyn, M. M. Murnane, and G. F. Mancini, "Subwavelength coherent imaging of periodic samples using a 13.5 nm tabletop high-harmonic light source," Nat. Photonics **11**, 259 (2017).
9. A. M. Maiden and J. M. Rodenburg, "An improved ptychographical phase retrieval algorithm for diffractive imaging," Ultramicroscopy **109**, 1256–1262 (2009).
10. A. M. Maiden, J. M. Rodenburg, and M. J. Humphry, "Optical ptychography: a practical implementation with useful resolution," Opt. Lett. **35**, 2585–2587 (2010).
11. A. M. Maiden, M. J. Humphry, F. Zhang, and J. M. Rodenburg, "Superresolution imaging via ptychography," JOSA A **28**, 604–612 (2011).
12. S. Gao, P. Wang, F. Zhang, G. T. Martinez, P. D. Nellist, X. Pan, and A. I. Kirkland, "Electron ptychographic microscopy for three-dimensional imaging," Nat. Commun. **8**, 163 (2017).
13. Y. Jiang, Z. Chen, Y. Han, P. Deb, H. Gao, S. Xie, P. Purohit, M. W. Tate, J. Park, S. M. Gruner, V. Elser, and D. A. Muller, "Electron ptychography of 2D materials to deep sub-ångström resolution," Nature **559**, 343 (2018).
14. M. Humphry, B. Kraus, A. Hurst, A. Maiden, and J. Rodenburg, "Ptychographic electron microscopy using high-angle dark-field scattering for sub-nanometre resolution imaging," Nat. Commun. **3**, 730 (2012).
15. K. Giewekemeyer, P. Thibault, S. Kalbfleisch, A. Beerlink, C. M. Kewish, M. Dierolf, F. Pfeiffer, and T. Salditt, "Quantitative biological imaging by ptychographic X-ray diffraction microscopy," Proc. Natl. Acad. Sci. U. S. A. **107**, 529–534 (2010).
16. M. Dierolf, P. Thibault, A. Menzel, C. M. Kewish, K. Jefimovs, I. Schlichting, K. Von Koenig, O. Bunk, and F. Pfeiffer, "Ptychographic coherent diffractive imaging of weakly scattering specimens," New J. Phys. **12**, 035017 (2010).
17. C. T. Putkunz, J. N. Clark, D. J. Vine, G. J. Williams, M. A. Pfeifer, E. Balaur, I. McNulty, K. A. Nugent, and A. G. Peele, "Phase-diverse coherent diffractive imaging: High sensitivity with low dose," Phys. Rev. Lett. **106**, 013903 (2011).

18. D. A. Shapiro, Y.-S. Yu, T. Tyliszczak, J. Cabana, R. Celestre, W. Chao, K. Kaznatcheev, A. D. Kilcoyne, F. Maia, S. Marchesini, Y. S. Meng, T. Warwick, L. L. Yang, and H. A. Padmore, "Chemical composition mapping with nanometre resolution by soft X-ray microscopy," Nat. Photonics **8**, 765–769 (2014).
19. M. Guizar-Sicairos and J. R. Fienup, "Phase retrieval with transverse translation diversity: a nonlinear optimization approach," Opt. Express **16**, 7264–7278 (2008).
20. P. Thibault, M. Dierolf, O. Bunk, A. Menzel, and F. Pfeiffer, "Probe retrieval in ptychographic coherent diffractive imaging," Ultramicroscopy **109**, 338–343 (2009).
21. M. Odstrčil, P. Baksh, S. Boden, R. Card, J. Chad, J. Frey, and W. Brocklesby, "Ptychographic coherent diffractive imaging with orthogonal probe relaxation," Opt. Express **24**, 8360–8369 (2016).
22. M. Odstrčil, A. Menzel, and M. Guizar-Sicairos, "Iterative least-squares solver for generalized maximum-likelihood ptychography," Opt. Express **26**, 3108–3123 (2018).
23. A. Maiden, M. Humphry, M. Sarahan, B. Kraus, and J. Rodenburg, "An annealing algorithm to correct positioning errors in ptychography," Ultramicroscopy **120**, 64–72 (2012).
24. F. Zhang, I. Peterson, J. Vila-Comamala, A. Diaz, F. Berenguer, R. Bean, B. Chen, A. Menzel, I. K. Robinson, and J. M. Rodenburg, "Translation position determination in ptychographic coherent diffraction imaging," Opt. Express **21**, 13592–13606 (2013).
25. J. Sun, Q. Chen, Y. Zhang, and C. Zuo, "Efficient positional misalignment correction method for Fourier ptychographic microscopy," Biomed. Opt. **7**, 1336–1350 (2016).
26. P. Thibault and A. Menzel, "Reconstructing state mixtures from diffraction measurements," Nature **494**, 68–71 (2013).
27. D. J. Batey, D. Claus, and J. M. Rodenburg, "Information multiplexing in ptychography," Ultramicroscopy **138**, 13–21 (2014).
28. R. Karl, C. Bevis, R. Lopez-Rios, J. Reichanadter, D. Gardner, C. Porter, E. Shanblatt, M. Tanksalvala, G. F. Mancini, M. Murnane, H. Kapteyn, and D. Adams, "Spatial, spectral, and polarization multiplexed ptychography," Opt. Express **23**, 30250–30258 (2015).
29. P. Thibault and M. Guizar-Sicairos, "Maximum-likelihood refinement for coherent diffractive imaging," New J. Phys. **14**, 063004 (2012).
30. A. M. Maiden, M. J. Humphry, and J. M. Rodenburg, "Ptychographic transmission microscopy in three dimensions using a multi-slice approach," J. Opt. Soc. Am. A **29**, 1606–1614 (2012).
31. E. H. Tsai, I. Usov, A. Diaz, A. Menzel, and M. Guizar-Sicairos, "X-ray ptychography with extended depth of field," Opt. Express **24**, 29089–29108 (2016).
32. C. M. Kewish, M. Guizar-Sicairos, C. Liu, J. Qian, B. Shi, C. Benson, A. M. Khounsary, J. Vila-Comamala, O. Bunk, J. R. Fienup, A. T. Macrander, and L. Assoufid, "Reconstruction of an astigmatic hard X-ray beam and alignment of KB mirrors from ptychographic coherent diffraction data," Opt. Express **18**, 23420–23427 (2010).
33. J. Vila-Comamala, A. Diaz, M. Guizar-Sicairos, A. Mantion, C. M. Kewish, A. Menzel, O. Bunk, and C. David, "Characterization of high-resolution diffractive X-ray optics by ptychographic coherent diffractive imaging," Opt. Express **19**, 21333–21344 (2011).
34. A. Schropp, R. Hoppe, V. Meier, J. Patommel, F. Seiboth, H. J. Lee, B. Nagler, E. C. Galtier, B. Arnold, U. Zastrau, J. Hastings, D. Nilsson, F. Uhlen, U. Vogt, H. M. Hertz, and S. Christian, "Full spatial characterization of a nanofocused X-ray free-electron laser beam by ptychographic imaging," Sci. Rep. **3**, 1633 (2013).
35. S. Hönig, R. Hoppe, J. Patommel, A. Schropp, S. Stephan, S. Schöder, M. Burghammer, and C. G. Schroer, "Full optical characterization of coherent x-ray nanobeams by ptychographic imaging," Opt. Express **19**, 16324–16329 (2011).
36. X. Huang, M. Wojcik, N. Burdet, I. Peterson, G. R. Morrison, D. J. Vine, D. Legnini, R. Harder, Y. S. Chu, and I. K. Robinson, "Quantitative X-ray wavefront measurements of fresnel zone plate and KB mirrors using phase retrieval," Opt. Express **20**, 24038–24048 (2012).
37. A. Schropp, P. Boye, J. Feldkamp, R. Hoppe, J. Patommel, D. Samberg, S. Stephan, K. Giewekemeyer, R. Wilke, T. Salditt, J. Gulden, A. P. Mancuso, I. A. Vartanyants, E. Weckert, S. M. Schoder, Burghammer, and C. G. Schroer, "Hard x-ray nanobeam characterization by coherent diffraction microscopy," Appl. Phys. Lett **96**, 091102 (2010).
38. X. Huang, H. Yan, E. Nazaretski, R. Conley, N. Bouet, J. Zhou, K. Lauer, L. Li, D. Eom, D. Legnini, R. Harder, I. K. Robinson, and Y. S. Chu, "11 nm hard X-ray focus from a large-aperture multilayer Laue lens," Sci. Rep. **3**, 3562 (2013).
39. J. Deng, D. J. Vine, S. Chen, Y. S. Nashed, Q. Jin, N. W. Phillips, T. Peterka, R. Ross, S. Vogt, and C. J. Jacobsen, "Simultaneous cryo X-ray ptychographic and fluorescence microscopy of green algae," Proc. Natl. Acad. Sci. U. S. A. **112**, 2314–2319 (2015).
40. J. Deng, D. J. Vine, S. Chen, Q. Jin, Y. S. Nashed, T. Peterka, S. Vogt, and C. Jacobsen, "X-ray ptychographic and fluorescence microscopy of frozen-hydrated cells using continuous scanning," Sci. Rep. **7**, 445 (2017).
41. J. Deng, Y. H. Lo, M. Gallagher-Jones, S. Chen, A. Pryor, Q. Jin, Y. P. Hong, Y. S. Nashed, S. Vogt, J. Miao, and C. Jacobsen, "Correlative 3D x-ray fluorescence and ptychographic tomography of frozen-hydrated green algae," Sci. Adv. **4**, eaau4548 (2018).
42. F. Seiboth, A. Schropp, M. Scholz, F. Wittwer, C. Rödel, M. Wünsche, T. Ullsperger, S. Nolte, J. Rahomäki, K. Parfeniukas, S. Giakoumidis, U. Vogt, U. Wagner, C. Rau, U. Boesenberg, J. Garrevoet, G. Falkenberg, E. C. Galtier, H. J. Lee, B. Nagler, and C. G. Schroer, "Perfect X-ray focusing via fitting corrective glasses to aberrated

optics," Nat. Commun. **8**, 14623 (2017).

43. P. Li, T. B. Edo, and J. M. Rodenburg, "Ptychographic inversion via wigner distribution deconvolution: Noise suppression and probe design," Ultramicroscopy **147**, 106–113 (2014).

44. J. C. da Silva and A. Menzel, "Elementary signals in ptychography," Opt. Express **23**, 33812–33821 (2015).

45. S. Marchesini, Y.-C. Tu, and H. Wu, "Alternating projection, ptychographic imaging and phase synchronization," Appl. Comput. Harmon. Analysis **41**, 815–851 (2015).

46. S. Marchesini and A. Sakdinawat, "Shaping coherent x-rays with binary optics," Opt. Express **27**, 907–917 (2019).

47. M. Guizar-Sicairos, M. Holler, A. Diaz, J. Vila-Comamala, O. Bunk, and A. Menzel, "Role of the illumination spatial-frequency spectrum for ptychography," Phys. Rev. B **86**, 100103 (2012).

48. A. Maiden, G. Morrison, B. Kaulich, A. Gianoncelli, and J. Rodenburg, "Soft X-ray spectromicroscopy using ptychography with randomly phased illumination," Nat. Commun. **4**, 1669 (2013).

49. M. Stockmar, P. Cloetens, I. Zanette, B. Enders, M. Dierolf, F. Pfeiffer, and P. Thibault, "Near-field ptychography: phase retrieval for inline holography using a structured illumination," Sci. Rep. **3**, 1927 (2013).

50. P. Li, D. J. Batey, T. B. Edo, A. D. Parsons, C. Rau, and J. M. Rodenburg, "Multiple mode X-ray ptychography using a lens and a fixed diffuser optic," J. Opt. **18**, 054008 (2016).

51. G. Morrison, F. Zhang, A. Gianoncelli, and I. Robinson, "X-ray ptychography using randomized zone plates," Opt. Express **26**, 14915–14927 (2018).

52. V. Guzenko, J. Romijn, J. Vila-Comamala, S. Gorelick, and C. David, "Efficient e-beam lithography exposure strategies for diffractive X-ray optics," in *AIP Conference Proceedings,* (AIP, 2011), pp. 92–95.

53. S. Gorelick, V. A. Guzenko, J. Vila-Comamala, and C. David, "Direct e-beam writing of dense and high aspect ratio nanostructures in thick layers of pmma for electroplating," Nanotechnology **21**, 295303 (2010).

54. M. Guizar-Sicairos, I. Johnson, A. Diaz, M. Holler, P. Karvinen, H.-C. Stadler, R. Dinapoli, O. Bunk, and A. Menzel, "High-throughput ptychography using Eiger: scanning X-ray nano-imaging of extended regions," Opt. Express **22**, 14859–14870 (2014).

55. C. Jacobsen, J. Deng, and Y. Nashed, "Strategies for high-throughput focused-beam ptychography," J. Synchrotron Radiat. **24**, 1078–1081 (2017).

56. D. Vine, D. Pelliccia, C. Holzner, S. B. Baines, A. Berry, I. McNulty, S. Vogt, A. G. Peele, and K. A. Nugent, "Simultaneous X-ray fluorescence and ptychographic microscopy of cyclotella meneghiniana," Opt. Express **20**, 18287–18296 (2012).

57. A. Diaz, P. Trtik, M. Guizar-Sicairos, A. Menzel, P. Thibault, and O. Bunk, "Quantitative X-ray phase nanotomography," Phys. Rev. B **85**, 020104 (2012).

58. T. Godden, A. Muñiz-Piniella, J. Claverley, A. Yacoot, and M. Humphry, "Phase calibration target for quantitative phase imaging with ptychography," Opt. Express **24**, 7679–7692 (2016).

59. X. Huang, H. Yan, R. Harder, Y. Hwu, I. K. Robinson, and Y. S. Chu, "Optimization of overlap uniformness for ptychography," Opt. Express **22**, 12634–12644 (2014).

60. O. Bunk, M. Dierolf, S. Kynde, I. Johnson, O. Marti, and F. Pfeiffer, "Influence of the overlap parameter on the convergence of the ptychographical iterative engine," Ultramicroscopy **108**, 481–487 (2008).

61. M. Odstrcil and M. Holler, "X-ray dataset for Illumination improvements for high-resolution ptychography," http://dx.doi.org/10.5281/zenodo.2639759 (2019).

62. R. M. Goldstein, H. A. Zebker, and C. L. Werner, "Satellite radar interferometry: Two-dimensional phase unwrapping," Radio Sci. **23**, 713–720 (1988).

63. J. Elam, D. Routkevitch, P. Mardilovich, and S. George, "Conformal coating on ultrahigh-aspect-ratio nanopores of anodic alumina by atomic layer deposition," Chem. Mater **15**, 3507–3517 (2003).

64. M. Van Heel and M. Schatz, "Fourier shell correlation threshold criteria," J. Struct. Biol. **151**, 250–262 (2005).

65. R. Cerbino, L. Peverini, M. Potenza, A. Robert, P. Bösecke, and M. Giglio, "X-ray-scattering information obtained from near-field speckle," Nat. Phys. **4**, 238–243 (2008).

66. R. M. Clare, M. Stockmar, M. Dierolf, I. Zanette, and F. Pfeiffer, "Characterization of near-field ptychography," Opt. Express **23**, 19728–19742 (2015).

67. M. Odstrčil, M. Lebugle, T. Lachat, J. Raabe, and M. Holler, "Fast positioning for X-ray scanning microscopy by a combined motion of sample and beam defining optics," J. Synchrotron Radiat. **26**, 504–509 (2019).

68. D. A. Shapiro, R. Celestre, P. Denes, M. Farmand, J. Joseph, A. Kilcoyne, S. Marchesini, H. Padmore, S. V. Venkatakrishnan, T. Warwick, and Y.-S. Yu, "Ptychographic Imaging of Nano-Materials at the Advanced Light Source with the Nanosurveyor Instrument," J. Phys.: Conf. Ser. **849**, 012028 (2017).

69. T. Edo, D. Batey, A. Maiden, C. Rau, U. Wagner, Z. Pešić, T. Waigh, and J. Rodenburg, "Sampling in x-ray ptychography," Phys. Rev. A **87**, 053850 (2013).

70. I. Mohacsi, I. Vartiainen, M. Guizar-Sicairos, P. Karvinen, V. A. Guzenko, E. Müller, E. Färm, M. Ritala, C. M. Kewish, A. Somogyi, and C. David, "High resolution double-sided diffractive optics for hard X-ray microscopy," Opt. Express **23**, 776–786 (2015).

71. I. Mohacsi, I. Vartiainen, B. Rösner, M. Guizar-Sicairos, V. A. Guzenko, I. McNulty, R. Winarski, M. V. Holt, and C. David, "Interlaced zone plate optics for hard X-ray imaging in the 10 nm range," Sci. Rep. **7**, 43624 (2017).

72. M. Haider, S. Uhlemann, E. Schwan, H. Rose, B. Kabius, and K. Urban, "Electron microscopy image enhanced," Nature **392**, 768–769 (1998).

73. P. Batson, N. Dellby, and O. Krivanek, "Sub-ångstrom resolution using aberration corrected electron optics," Nature

418, 617–620 (2002).

74. J. Verbeeck, A. Béché, K. Müller-Caspary, G. Guzzinati, M. A. Luong, and M. Den Hertog, "Demonstration of a 2× 2 programmable phase plate for electrons," Ultramicroscopy **190**, 58–65 (2018).

75. J. Verbeeck, H. Tian, and P. Schattschneider, "Production and application of electron vortex beams," Nature **467**, 301 (2010).

76. T. R. Harvey, J. S. Pierce, A. K. Agrawal, P. Ercius, M. Linck, and B. J. McMorran, "Efficient diffractive phase optics for electrons," New J. Phys. **16**, 093039 (2014).

77. G. Zheng, R. Horstmeyer, and C. Yang, "Wide-field, high-resolution Fourier ptychographic microscopy," Nat. Photon. **7**, 739–745 (2013).

78. K. Wakonig, A. Diaz, A. Bonnin, M. Stampanoni, A. Bergamaschi, J. Ihli, M. Guizar-Sicairos, and A. Menzel, "X-ray Fourier ptychography," Sci. Adv **5**, 0282 (2019).